CrossMark

J. Fluid Mech. (2015), *vol.* 780, *pp.* 120–142. © Cambridge University Press 2015
doi:10.1017/jfm.2015.460

Actively flapping tandem flexible flags in a viscous flow

Emad Uddin[1,‡], Wei-Xi Huang[2,†] and Hyung Jin Sung[1,†]

[1]Department of Mechanical Engineering, KAIST, 291 Daehak-ro, Yuseong-gu, Daejeon 34141, Korea

[2]Department of Engineering Mechanics, Tsinghua University, Beijing 100084, China

(Received 9 September 2014; revised 17 June 2015; accepted 2 August 2015;
first published online 2 September 2015)

The active flapping motions of fish and cetaceans generate both propulsive and manoeuvring forces. The tail fin motions of the majority of fish can essentially be viewed as a combined pitch-and-heave motion. Downstream bodies are strongly influenced by the vortices shed from an upstream body. To investigate the interactions between flexible bodies and vortices, the present study examined tandem flexible flags in a viscous flow by using an improved version of the immersed boundary method. The upstream flag underwent passive flapping in a uniform flow while the downstream flag flapped according to a prescribed pitching and heaving motion of the leading edge. The influences of the active flapping motion on the system dynamics were examined in detail, including the frequency, the phase angle, the bending coefficient and the amplitudes of the pitching and heaving motion. The variation of the drag coefficient of the downstream flag was explored together with the instantaneous vorticity contours and the body shapes. Both the slalom mode and the interception mode were identified according to the vortex–flexible body interactions, corresponding to the low- and high-drag situations, respectively. The underlying mechanism was discussed and compared with previous studies.

Key words: flow–structure interactions, swimming/flying, vortex interactions

1. Introduction

The flapping of wings during flight or fins during swimming presents an intriguing system from which to understand the interactions between a moving structure and the surrounding fluid. In aquatic environments natural selection has driven physiological development to optimize the efficiency of flapping locomotion, which can be viewed essentially as a combined pitch-and-heave motion in most cases (Akhtar, Mittal & Lauder 2007). Previous theoretical and experimental studies have emphasized the potential for wake interactions among nearby fish or fins to increase the propulsive efficiency (Spagnolie *et al.* 2010). Such interactions include high complexities and have not yet been well understood from a hydrodynamics perspective, and a more detailed study would be highly desirable (Fish & Lauder 2006; Wu 2011).

† Email address for correspondence: hjsung@kaist.ac.kr
‡ Present address: Department of Mechanical Engineering, SMME, NUST H-12, Islamabad 46000, Pakistan.

https://doi.org/10.1017/jfm.2015.460 Published online by Cambridge University Press

An illuminating approach to studying vortex dynamics during swimming has involved characterizing the system dynamics of a flag-in-flow problem and evaluating the effects of certain key parameters: the mass ratio, the bending rigidity and the Reynolds number (Zhang *et al.* 2000; Shelley & Zhang 2011). Passively flapping systems have been shown to share some essential features of the active swimming problem, including the fluid–flexible body interactions, lending insight into how the flexibility of a fish (flag) affects the swimming efficiency. The effects of oncoming vortices are considered by numerically and experimentally studying the flow past flags in a tandem arrangement (Jia & Yin 2008; Ristroph & Zhang 2008; Alben 2009; Zhu 2009; Kim, Huang & Sung 2010). Interestingly, the downstream filament may experience a higher drag force than was experienced by the upstream flag or a single-filament system (Ristroph & Zhang 2008). Kim *et al.* (2010) examined the constructive and destructive modes of the vortex interactions in flag wakes corresponding to inverted or normal drafting, respectively, at different streamwise gap distances (Gopalkrishnan *et al.* 1994). A downstream flag that is allowed to move freely in the lateral direction can effectively utilize the oncoming vortices in a slalom manner (Jia & Yin 2008). As a result, the downstream flag extracts energy from the wake and receives an increased drag force. In live fish systems, Liao *et al.* (2003) demonstrated that a trout swimming in the wake of a stationary object placed in a water flow can exploit the oncoming vortices to reduce the muscle force and energy cost of locomotion. Beal *et al.* (2006) showed that dead fish can extract energy from oncoming vortices in the wake of a bluff cylinder by engaging in a passive flapping motion that overcomes the drag force and generates a thrust force.

As a simple model of the flying/swimming problem, flow around actively flapping foils has been extensively studied (Wang 2005; Lauder *et al.* 2007; Shyy 2010; Deng *et al.* 2013). A foil experiencing a combination of harmonic pitching and heaving motions produces a thrust force through the formation of a jet-like flow that projects downstream from the trailing edge of the foil (Anderson *et al.* 1998). The pitching oscillation was found to play a major role in the production of thrust, which can be understood by considering the wings of an insect during hovering flight (Guglielmini & Blondeaux 2004). The propulsion efficiency is maximized if there is a phase lag of about 90° between the pitching motion and the heaving motion (Lighthill 1970; Tuncer & Kaya 2005). Recently, a passively deformable airfoil or plate attracted more attention to the influence of flexibility in a flapping wing or fin on the flying/swimming performance, e.g. thrust generation, efficiency enhancement and wake symmetry, and the underlying mechanisms (Alben, Madden & Lauder 2007; Michelin & Smith 2009; Masoud & Alexeev 2010; Thiria & Godoy-diana 2010; Alben 2011; Kang *et al.* 2011; Ramananarivo, Godoy-diana & Thiria 2011; Alben, Witt & Baker 2012; Eloy & Lauga 2012; Marais *et al.* 2012; Shoele & Zhu 2012; Uddin, Huang & Sung 2013; Zhu, He & Zhang 2014*a*,*b*). Studies on the behaviours of an actively flapping body under the influence of oncoming vortices are relatively scarce. The presence of vortices introduces more complicated interactions, but constitutes an important means of understanding the hydrodynamic properties of fish schooling, bird flocking and interactions among wings/fins. Lauder *et al.* (2007) developed a dual-foil flapping robotic device as an interaction model of dorsal and caudal fins, which can be used to improve our understanding of the significance of flexibility in the locomotion performance. Zhu, He & Zhang (2014*c*) simulated the motions of two tandem self-propelled filaments in viscous fluid. They found that the equilibrium separation distance of the two tandem flags is closely correlated with the streamwise spacing of the reversed Karman vortex behind the upstream

https://doi.org/10.1017/jfm.2015.460 Published online by Cambridge University Press

filament. The head of the downstream filament is prone to swim through the cores of oncoming positive and negative vortices alternately to obtain energetic benefits, which is different from the slalom motion between oncoming vortex cores as reported in Liao *et al.* (2003) and Jia & Yin (2008).

In the present study, the dynamics of flow around a pair of coupled flexible flags arranged tandemly and subjected to a uniform flow was investigated. The upstream flexible flag passively flapped while the downstream flexible flag flapped according to the active pitching and heaving motions of its leading edge. Actively flapping downstream flexible flags are common in nature, for example among swimming fish, but the flapping mode, interaction modes and optimal flapping conditions are not yet well understood. The current study provides necessary insights towards better understanding of the manoeuvring dynamics of actively flapping flexible bodies in a viscous flow or the swimming behaviour of fish. The drag coefficient of the actively flapping downstream flexible flag depended on the frequency, phase angles and amplitudes of the pitching and heaving motions, and the bending coefficient. These dependences were examined in detail. Some intriguing results were obtained: within a range of the flapping parameters, the actively flapping downstream flag experienced a distinct reduction or enhancement of the drag coefficient. The vortices shed from the upstream flag interacting with the downstream flag in different modes were identified, and the underlying mechanism of the drag variation was explored. The next section introduces the formulation of the problem, and a description of the computational configuration is provided. Section 3 presents the numerical results and discussion. Finally, conclusions are drawn in § 4.

2. Computational model

In the present study, a grouping unit consisting of two flexible bodies was modelled using two tandem flexible flags in a uniform flow. A schematic diagram of the computational configuration, together with the coordinate system, is shown in figure 1. The relative positions of the two tandem flags were varied by adjusting the initial streamwise gap distance G_x. The leading edge of the upstream flag was fixed, whereas a pitching and heaving motion was prescribed for the head of the downstream flag. An Eulerian coordinate system was used to describe the fluid flow, and a separate Lagrangian coordinate system was applied to each flexible flag. The fluid–flag coupling system was modelled using an improved version of the immersed boundary method (Huang, Shin & Sung 2007). According to this method the fluid flow and the flag motions were solved separately in each coordinate system, and the fluid–flag interactions were calculated using a feedback force. Huang *et al.* (2007) simulated a single flexible flag and two flags in a side-by-side arrangement in a uniform flow, assuming that the flags were inextensible. Because the same method was used here, with the only difference being the mutual arrangement of the flags, the validity of the numerical results will be assumed in the following discussion.

The incompressible viscous fluid flow was described using the Navier–Stokes and continuity equations, which were non-dimensionalized by choosing the far-field velocity U_∞ and the flag length L as the characteristic scales, i.e.,

$$\frac{\partial \boldsymbol{u}}{\partial t} + \boldsymbol{u}\cdot\nabla\boldsymbol{u} = -\nabla p + \frac{1}{Re}\nabla^2\boldsymbol{u} + \boldsymbol{f}, \tag{2.1}$$

$$\nabla\cdot\boldsymbol{u} = 0. \tag{2.2}$$

Here, the Reynolds number was defined by $Re = \rho_0 U_\infty L/\mu$, where ρ_0 is the fluid density and μ is the dynamic viscosity. As in the method described by

https://doi.org/10.1017/jfm.2015.460 Published online by Cambridge University Press

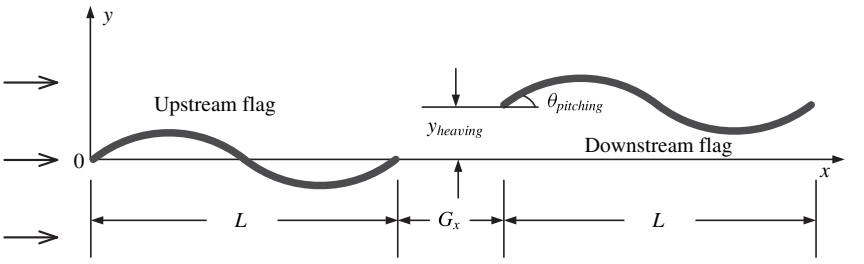


FIGURE 1. Schematic diagram showing the two tandem flags in a uniform flow, where the head of the downstream flag was prescribed with active pitching and heaving motions. $y_{heaving} = Y\cos(\omega t - \Phi_{heaving})$; $\theta_{pitching} = \Phi\cos(\omega t - \Phi_{pitching})$.

Huang *et al.* (2007), the governing equations for the inextensible flexible flag were non-dimensionalized using the following characteristic scales: L for the length, L/U_∞ for the time, $\rho_1 U_\infty^2/L$ for the Lagrangian force $\boldsymbol{F}$, $\rho_1 U_\infty^2$ for the tension force T and $\rho_1 U_\infty^2 L^2$ for the bending rigidity γ, where ρ_1 denotes the density difference between the flag and the surrounding fluid. The flexible flag was, therefore, described by

$$\frac{\partial^2 \boldsymbol{X}}{\partial t^2} = \frac{\partial}{\partial s}\left(T\frac{\partial \boldsymbol{X}}{\partial s}\right) - \frac{\partial^2}{\partial s^2}\left(\gamma\frac{\partial^2 \boldsymbol{X}}{\partial s^2}\right) - \boldsymbol{F}, \tag{2.3}$$

$$\frac{\partial \boldsymbol{X}}{\partial s}\cdot\frac{\partial \boldsymbol{X}}{\partial s} = 1, \tag{2.4}$$

where s is the arclength and $\boldsymbol{X} = (X(s,t), Y(s,t))$ is the position. The tension force T is determined by the constraint of inextensibility and is a function of s and t, while the bending rigidity γ is assumed to be constant. At the fixed end of the upstream flag, the simply supported boundary conditions were applied, i.e.,

$$\boldsymbol{X} = \boldsymbol{X}_0, \quad \frac{\partial^2 \boldsymbol{X}}{\partial s^2} = (0,0). \tag{2.5a,b}$$

At the free ends of the upstream and downstream flags, the boundary conditions were expressed as

$$T = 0, \quad \frac{\partial^2 \boldsymbol{X}}{\partial s^2} = (0,0), \quad \frac{\partial^3 \boldsymbol{X}}{\partial s^3} = (0,0). \tag{2.6a–c}$$

On the other hand, at the leading edge of the downstream flag, the clamped boundary conditions were adopted, i.e.,

$$\boldsymbol{X} = (x_1, y), \quad \frac{\partial \boldsymbol{X}}{\partial s} = (\cos\theta,\ \sin\theta). \tag{2.7a,b}$$

In the above equation, the normal position y and the inclination angle θ were attained according to the active pitching and heaving motions, i.e.,

$$y = Y\cos(\omega t - \Phi_{heaving}), \tag{2.8}$$

$$\theta = \Theta\cos(\omega t - \Phi_{pitching}), \tag{2.9}$$

where ω is the frequency of the pitching and heaving motions, $\Phi_{heaving}$ is the phase angle of the heaving motion and $\Phi_{pitching}$ is the phase angle of the pitching motion.

https://doi.org/10.1017/jfm.2015.460 Published online by Cambridge University Press

The interaction force between the flow and the structure was calculated using the feedback force,

$$\boldsymbol{F} = \alpha \int_0^t (\boldsymbol{U}_{ib} - \boldsymbol{U})\,\mathrm{d}t' + \beta(\boldsymbol{U}_{ib} - \boldsymbol{U}), \tag{2.10}$$

where α and β are large negative free constants set to be 10^5 and 10^3, respectively, as in Huang *et al.* (2007). $\boldsymbol{U}_{ib}$ is the fluid velocity obtained by interpolation at the immersed boundary, and $\boldsymbol{U}$ is the velocity of the flag expressed by $\boldsymbol{U} = \mathrm{d}\boldsymbol{X}/\mathrm{d}t$. The following interpolation relations between the Eulerian and Lagrangian variables were realized using the Dirac delta function, as described in Shin, Huang & Sung (2008):

$$\boldsymbol{U}_{ib}(s, t) = \int_\Omega \boldsymbol{u}(\boldsymbol{x}, t)\delta(\boldsymbol{X}(s, t) - \boldsymbol{x})\,\mathrm{d}\boldsymbol{x}, \tag{2.11}$$

$$\boldsymbol{f}(\boldsymbol{x}, t) = \rho \int_\Gamma \boldsymbol{F}(s, t)\delta(\boldsymbol{x} - \boldsymbol{X}(s, t))\,\mathrm{d}s, \tag{2.12}$$

where $\rho = \rho_1/\rho_0 L$ denotes the density ratio.

For numerical implementation, the fluid motion equations (2.1) and (2.2) were solved by using the fractional-step method with a staggered Cartesian grid system (Kim, Baek & Sung 2002). On the other hand, the finite difference method was adopted to calculate the solid motion equations (2.3) and (2.4). More details of the numerical schemes can be found in Huang *et al.* (2007). The overall computational process for simulating the fluid–flag coupling system is summarized as follows (Huang & Sung 2009):

(1) Initialize the computation parameters, the meshes and the fluid and solid motions; set $\boldsymbol{U}_{ib}^0 = \boldsymbol{U}^0$.
(2) At the nth time step, the fluid velocity $\boldsymbol{u}^n$ and the solid position $\boldsymbol{X}^n$ and velocity $\boldsymbol{U}^n$ are known. Interpolate the fluid velocity at the Lagrangian points to obtain $\boldsymbol{U}_{ib}^n$ and then calculate the Lagrangian momentum force $\boldsymbol{F}^n$.
(3) Map the Lagrangian momentum force onto the Eulerian grid. Obtain the updated fluid velocity field and pressure field.
(4) Substitute $\boldsymbol{F}^n$ into the flag motion equation and obtain the flag position at the new time step $\boldsymbol{X}^{n+1}$, as well as the velocity $\boldsymbol{U}^{n+1} = (\boldsymbol{X}^{n+1} - \boldsymbol{X}^n)/\Delta t$. Return to step (2) and march to the next time step.

The Eulerian grid size for the fluid was 512×250 and the Lagrangian grid size for each flag was 64. The Eulerian grid was uniformly distributed along the x and y directions over $-2 \leqslant y \leqslant 2$, but was stretched otherwise. The far-flow field conditions were applied at the top and bottom boundaries as well as at the inlet of the fluid domain, whereas the convective boundary conditions were used at the outlet. The computational time step was set to 0.0005, which resulted in a CFL number of about 0.1. The initial position of the upstream flag was parallel to the streamwise direction, while the downstream flag was inclined at a small angle relative to the streamwise direction. Although the initial inclination angle of the downstream flag was different from the prescribed pitching motion of the leading edge, the results after several transient periods remained unchanged. The dynamics of the system were investigated by conducting simulations over a long time period, between 100 and 500 flapping periods, and the flow data obtained after the establishment of a steadily flapping state were analysed. The flow patterns were characterized by the drag coefficient C_d, the

https://doi.org/10.1017/jfm.2015.460 Published online by Cambridge University Press

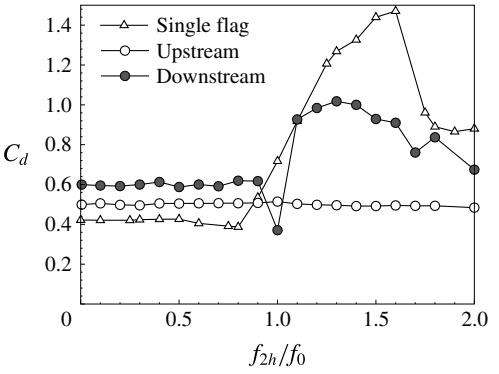


FIGURE 2. The drag coefficient as a function of the frequency ratio: $\gamma = 0.006$, $Re = 300$, $G_x = 1.0$, $\Theta = 0.1\pi$, $Y = 0.2$, $\Phi_{pitching} = 0.5\pi$, $\Phi_{heaving} = 0$.

Frequency ratio	$0 \leqslant f_{2h}/f_0 \leqslant 2.0$
Gap distance	$0.2 \leqslant G_x \leqslant 2.0$
Phase angle of the pitching motion	$0 \leqslant \Phi_{pitching} \leqslant 2\pi$
Phase angle of the heaving motion	$0 \leqslant \Phi_{heaving} \leqslant 2\pi$
Amplitude of the pitching motion	$0 \leqslant \Phi \leqslant 0.3\pi$
Amplitude of the heaving motion	$0 \leqslant Y \leqslant 0.6$
Bending coefficient	$10^{-4} \leqslant \gamma \leqslant 10^{-2}$

TABLE 1. The parameters in the present simulation.

evolution of the tail position, the power spectrum and the vorticity contours. Seven parameters were chosen to optimize the system configuration: the frequency ratio of the head of the downstream flag to the tail of the upstream flag (f_{2h}/f_0), the gap distance (G_x), the phase angles for the pitching and heaving motions ($\Phi_{pitching}$ and $\Phi_{heaving}$), the amplitudes of the pitching and heaving motions (Θ and Y) and the bending coefficient γ. The seven parameters lay within the ranges as listed in table 1. In the next section, we first examine the effects of the frequency ratio and the gap distance, then the variations of the phase angles as well as the flapping amplitudes, and finally the dependence of the results on the bending coefficient.

3. Results and discussion

In the simulations, the following parameters were first selected, i.e. $Re = 300$, the mass ratio $\rho = 1$, the pitching and heaving amplitudes $\Theta = 0.1\pi$ and $Y = 0.2$, the phase angles $\Phi_{pitching} = 0.5\pi$ and $\Phi_{heaving} = 0$, and the bending coefficient $\gamma = 0.006$. Figure 2 shows the averaged drag coefficient, C_d, of both the upstream and downstream flags as a function of the frequency ratio, f_{2h}/f_0, where the flapping frequency of the upstream flag was assumed to remain unchanged and equal to the natural frequency of the single flag ($f_0 = 0.31$). C_d of the single pitching and heaving flag was also included for comparison. The value of C_d of the upstream flag (C_{d1}) changed only very slightly with f_{2h}/f_0, indicating that the downstream flag exerted a negligible influence on the upstream flag. On the other hand, obvious changes of the downstream flag (C_{d2})

https://doi.org/10.1017/jfm.2015.460 Published online by Cambridge University Press

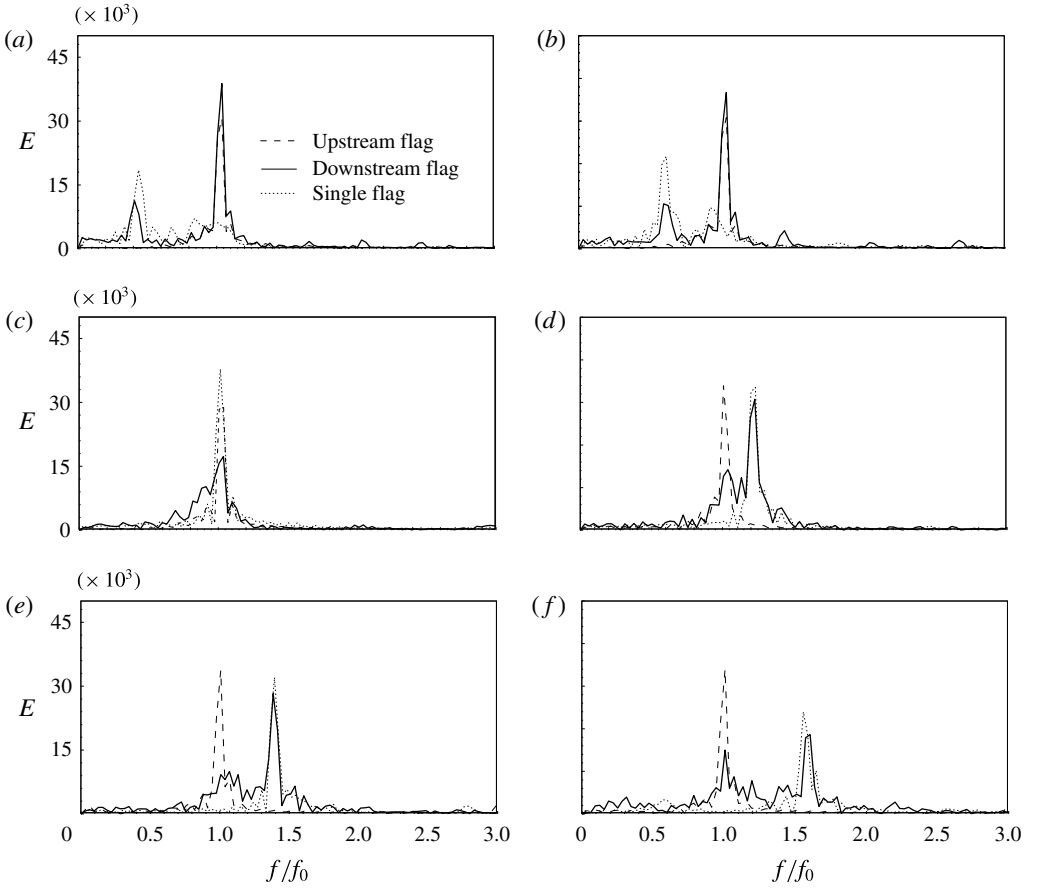


FIGURE 3. Power spectra of the tail positions as a function of the frequency ratio: (*a*) $f_{2h}/f_0 = 0.3$; (*b*) $f_{2h}/f_0 = 0.6$, $Re = 300$, $G_x = 1.0$, $\gamma = 0.006$; (*c*) $f_{2h}/f_0 = 1.0$, $\Theta = 0.1\pi$, $Y = 0.2$; (*d*) $f_{2h}/f_0 = 1.2$, $\Phi_{pitching} = 0.5\pi$, $\Phi_{heaving} = 0$; (*e*) $f_{2h}/f_0 = 1.4$; (*f*) $f_{2h}/f_0 = 1.6$.

were seen over the range $0 \leqslant f_{2h}/f_0 \leqslant 2.0$. As seen in figure 2, at low frequency ratios, i.e. $f_{2h}/f_0 < 1.0$, C_{d2} remained constant, slightly higher than the upstream one. At $f_{2h}/f_0 = 1.0$, a sudden decrease in C_{d2} was observed; then for $1.0 \leqslant f_{2h}/f_0 \leqslant 1.3$, C_{d2} increased significantly; for $f_{2h}/f_0 > 1.3$, C_{d2} decreased gradually. In figure 2, a similar trend was also observed for the single pitching and heaving flag, showing a sharp increase followed by a decrease in C_d, which was consistent with the experimental results obtained from an oscillating foil by Anderson *et al.* (1998). Nevertheless, there were some different behaviours between the single and tandem cases. For instance, C_d of the single pitching and heaving flag increased gradually within the vicinity of 1, rather than the sudden increase of the downstream flag. For $f_{2h}/f_0 > 1.3$, C_d of the single pitching and heaving flag decreased more sharply than in the tandem case. Such differences indicated that the vortices shed from the upstream flag influenced the downstream flag.

The power spectra of the tail positions at different frequency ratios are shown in figure 3. The dominant frequency of the upstream flag remained constant as f_{2h}/f_0 was varied. This dominant frequency was equal to the natural flapping frequency of the flag, whereas higher harmonics in the downstream flag were excited by the

https://doi.org/10.1017/jfm.2015.460 Published online by Cambridge University Press

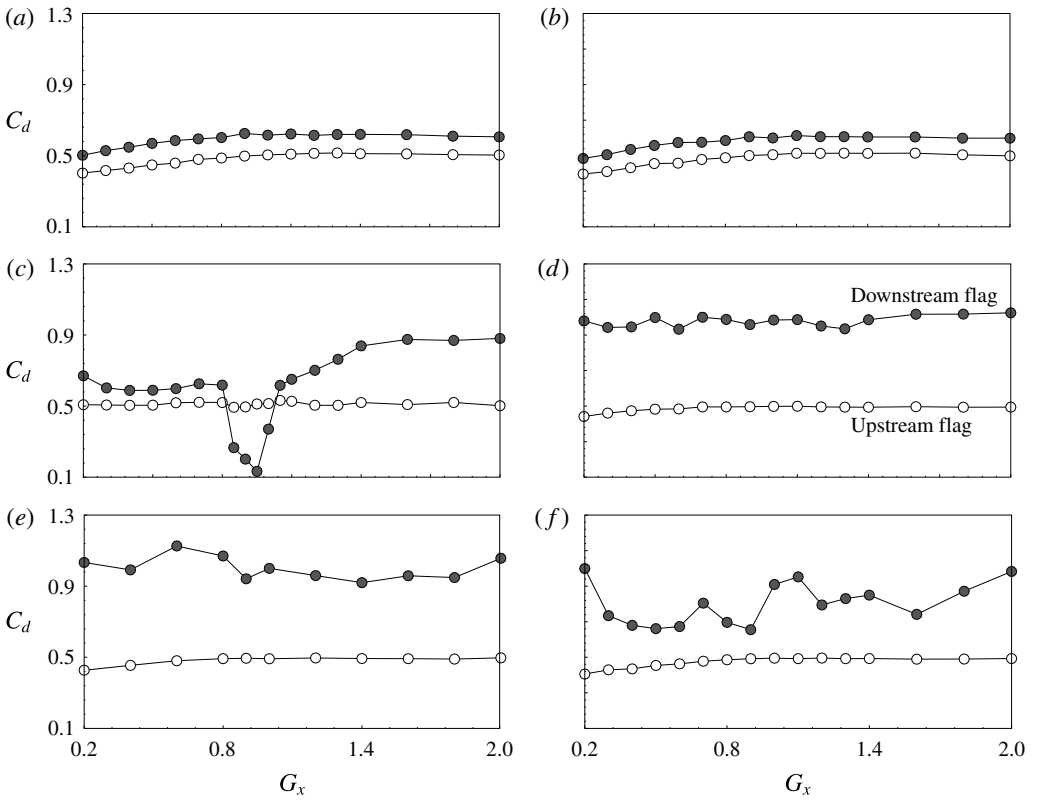


FIGURE 4. The drag coefficient as a function of the gap distance at different frequency ratios: (*a*) $f_{2h}/f_0 = 0.3$, $\Theta = 0.1\pi$, $\gamma = 0.2$; (*b*) $f_{2h}/f_0 = 0.6$, $Re = 300$, $Y = 0.006$; (*c*) $f_{2h}/f_0 = 1.0$, $\Phi_{pitching} = 0.5\pi$, $\Phi_{heaving} = 0$; (*d*) $f_{2h}/f_0 = 1.2$; (*e*) $f_{2h}/f_0 = 1.4$; (*f*) $f_{2h}/f_0 = 1.6$.

pitching and heaving motions. As seen in figure 3, two peaks in the spectra of the downstream flag were generally present: one corresponding to the natural flapping frequency f_0 and the other corresponding to the pitching and heaving frequency f_{2h}. For $f_{2h}/f_0 < 1.0$, the dominant frequency of the downstream flag was the natural flapping frequency f_0, whereas for $f_{2h}/f_0 > 1.0$, the pitching and heaving frequency f_{2h} became dominant. On the other hand, the dominant frequency for the single pitching and heaving flag was the imposed flapping frequency. For $f_{2h}/f_0 < 1.0$, a weak peak was present at the natural flapping frequency for the single flapping flag, which became invisible for $f_{2h}/f_0 > 1.0$. A comparison between the single and tandem cases revealed that the dominance of the natural flapping frequency of the downstream flag for $f_{2h}/f_0 < 1.0$ resulted from the vortices shed upstream, whereas the dominance of the imposed frequency for $f_{2h}/f_0 > 1.0$ arose from the energetic excitation exerted on the downstream flag by the actively flapping leading edge. The change in the dominant frequency of the downstream flag reflected a transition of the vortex–flag interaction modes, which sharply increased the drag of the downstream flag as the pitching and heaving frequency increased (figure 2).

Figure 4 shows the drag coefficient as a function of the gap distance (G_x) for different frequency ratios. At low frequency ratios, i.e., $f_{2h}/f_0 = 0.3$ and 0.6, the drag coefficient of the downstream flag, C_{d2}, was higher than that of the upstream

https://doi.org/10.1017/jfm.2015.460 Published online by Cambridge University Press

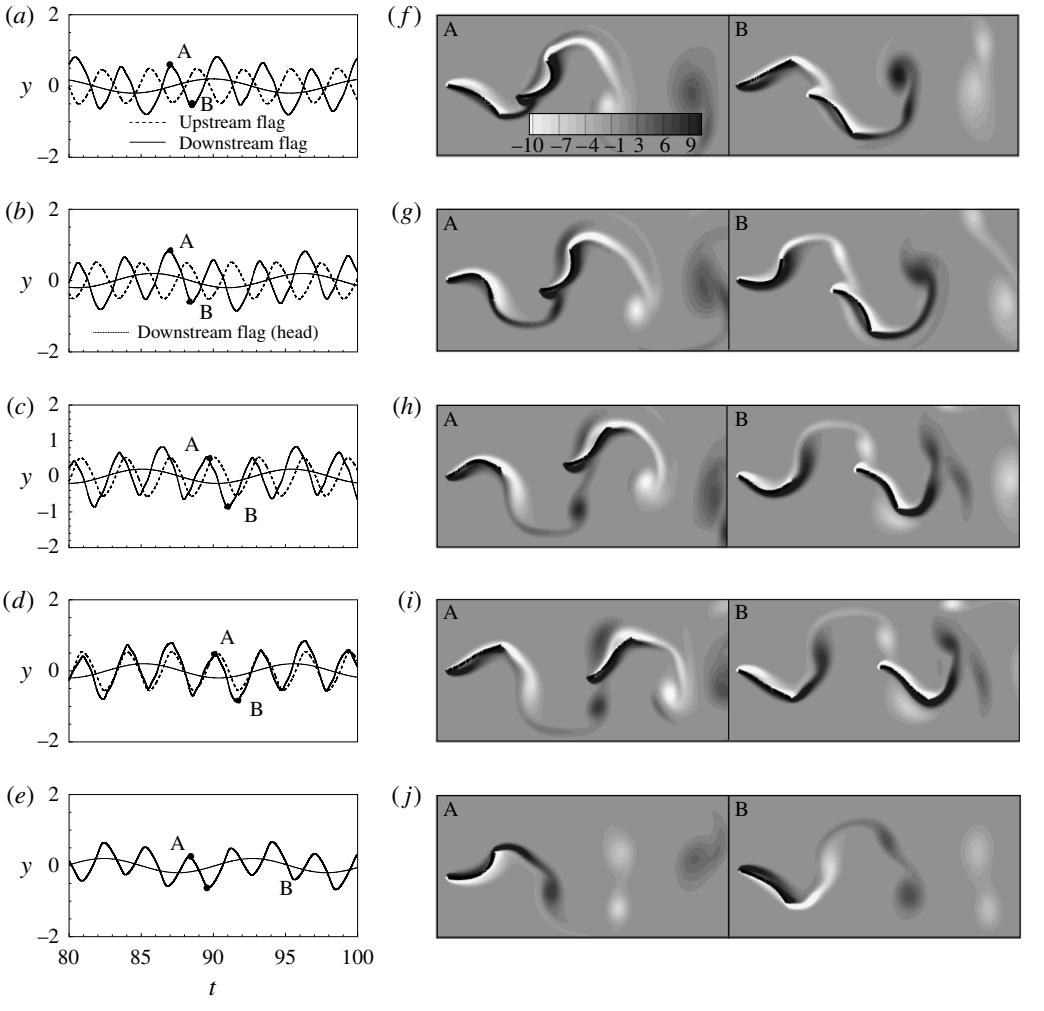


FIGURE 5. Time histories of the head and tail positions (*a–e*) and vorticity contours, together with the body shape (*f–j*) at $f_{2h}/f_0 = 0.3$: (*a*) $G_x = 0.2$; (*b*) $G_x = 0.6$; (*c*) $G_x = 1.0$; (*d*) $G_x = 1.4$; (*e*) $G_x = \infty$. Other parameters were $Re = 300$, $Y = 0.2$, $\Theta = 0.1\pi$, $\Phi_{pitching} = 0.5\pi$, $\Phi_{heaving} = 0$, $\gamma = 0.006$.

flag, C_{d1}. The drag forces changed only slightly as G_x was varied. Recall that in a system of two tandem flapping flags with fixed leading edges (Kim *et al.* 2010), both the constructive and destructive vortex interaction modes were present. The former was observed at $Re = 200$ for all gap distances, where the drag coefficient of the downstream flag was increased; the latter was observed at $Re = 400$, which induced a significant drag reduction of the downstream flag at certain gap distances. Here, the actively flapping flag at $Re = 300$ with low frequency ratios was similar to the constructive mode of the passively flapping flag.

The instantaneous vorticity contours at different gap distances and $f_{2h}/f_0 = 0.3$ are displayed in figure 5, together with the time histories of the head and tail positions of the flags. The upstream shedding vortices always interacted with the downstream flag in the constructive mode. Because the head of the downstream flag moved more

https://doi.org/10.1017/jfm.2015.460 Published online by Cambridge University Press

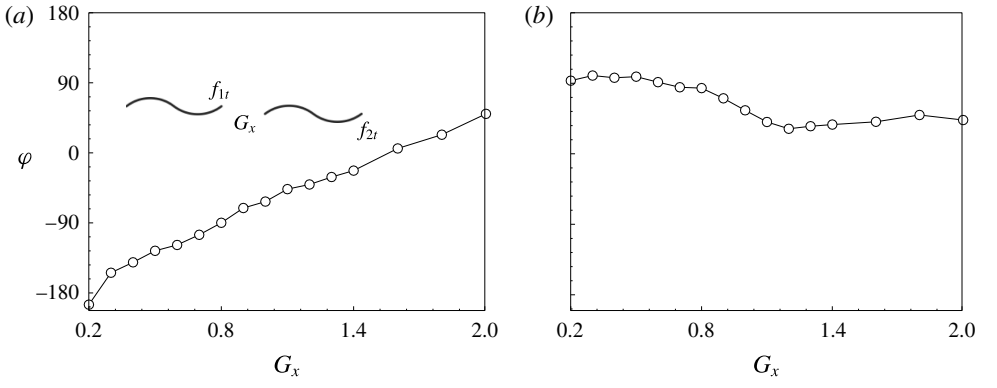


FIGURE 6. The phase difference between the tail positions of the downstream and upstream flags as a function of the frequency ratio: (*a*) $f_{2h}/f_0 = 0.3$; (*b*) $f_{2h}/f_0 = 1.0$. Other parameters are $Re = 300$, $Y = 0.2$, $\Phi = 0.1\pi$, $\Phi_{pitching} = 0.5\pi$, $\Phi_{heaving} = 0$, $\gamma = 0.006$.

slowly than the tail of the upstream flag, the flapping of the downstream flag was modulated by the upstream shedding vortices, as observed in the time histories of the tail positions. On the other hand, two pairs of vortices were shed in each flapping period from the single pitching and heaving flag at $f_{2h}/f_0 = 0.3$ (figure 5*e*), i.e. 2P mode (Williamson & Govardhan 2004). As a result of the vortex interactions, the flag that pitched and heaved at a low frequency behaved similarly to the passively flapping flags in a tandem arrangement. Additional evidence can be found in figure 6, which shows the phase difference between the tail positions of the upstream and downstream flags. For $f_{2h}/f_0 = 0.3$ (figure 6*a*), the phase difference increased linearly with the gap distance, which was proportional to the time required for the vortices shed upstream to arrive at the downstream flag, consistent with the passively flapping tandem flags (Kim *et al.* 2010).

At $f_{2h}/f_0 = 1.0$ the downstream flag experienced a significant drag reduction at the gap distance close to 1.0, as shown in figure 4(*c*). At this frequency ratio, the head of the downstream flag followed the tail of the upstream flag, as seen in the time histories of the tail positions in figure 7, whereas the tail of the downstream flag led by a phase angle. The phase angle was nearly constant ($\pi/2$) for small G_x, decreased to a small value when G_x was close to 1.0 and remained small as G_x increased further (figure 6*b*). The vorticity contours in figure 7(*a*) and (*b*) showed that the constructive mode was formed at small gap distances as the vortices were not fully detached from the upstream flag, like the case of $f_{2h}/f_0 = 0.3$. As G_x was close to 1.0 (figure 7*c*), the downstream flag passed in between the pairs of vortices shed from the upstream one, resulting in a slalom mode and a drag reduction of the downstream flag. As G_x increased further (figure 7*d*), the leading edge of the downstream flag always moved through one of the pair of vortices, resulting in an interception mode and a significant increase in drag.

Time evolution of the vorticity along the vertical line at the leading edge of the downstream flag is displayed in figure 8. The image was analogous to that recorded by a streak camera, and similar ones can be found in Jia & Yin (2008) and Zhu *et al.* (2014*c*). The direction of time advance was leftward, opposite to the incoming flow, so it looked as if the flag was swimming in a quiescent fluid. The results were clear in the sense that only the relative motion of the body to the surrounding fluid at a specific streamwise location was displayed. For reference, time evolution

https://doi.org/10.1017/jfm.2015.460 Published online by Cambridge University Press

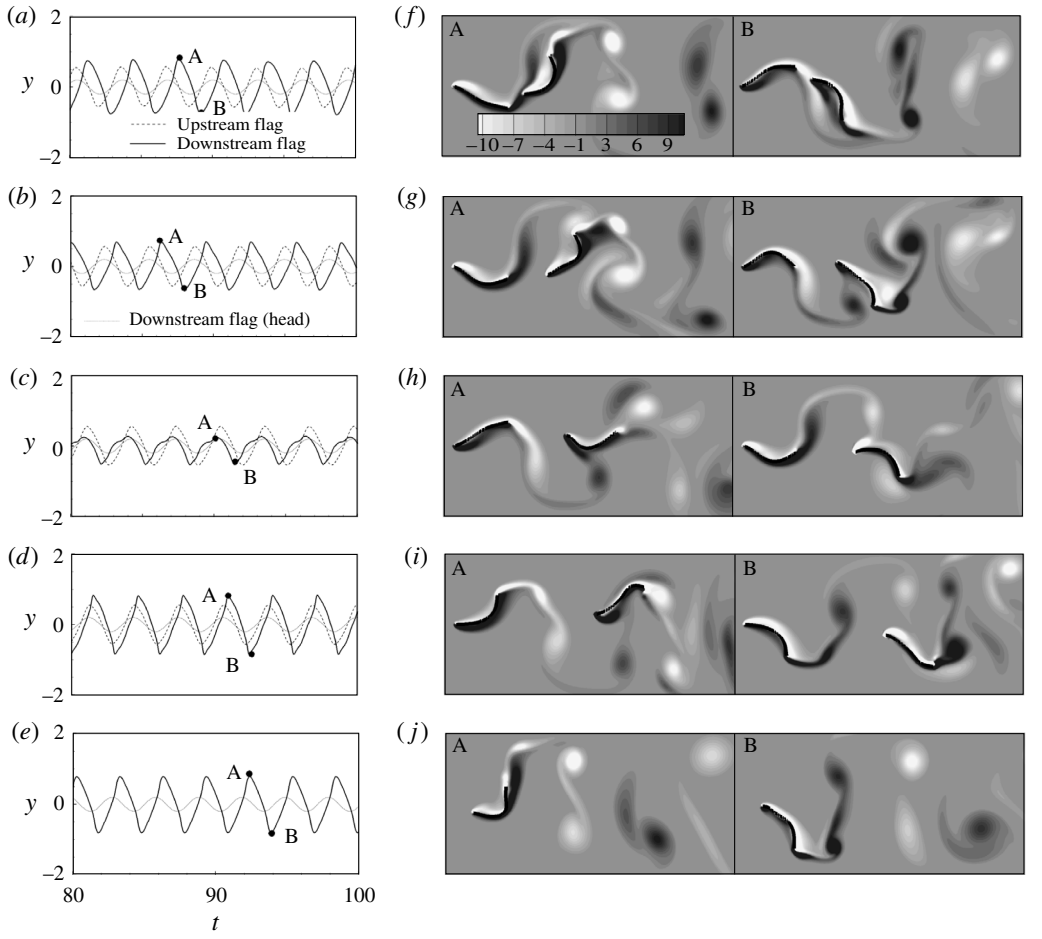


FIGURE 7. Time histories of the head and tail positions (*a–e*) and vorticity contours, together with the body shape (*f–j*) at $f_{2h}/f_0 = 1.0$ (rather than for $f_{2h}/f_0 = 0.3$, in figure 5): (*a*) $G_x = 0.2$; (*b*) $G_x = 0.6$; (*c*) $G_x = 0.9$; (*d*) $G_x = 1.4$; (*e*) $G_x = \infty$. Other parameters were $Re = 300$, $Y = 0.2$, $\Theta = 0.1\pi$, $\Phi_{pitching} = 0$, $\Phi_{heaving} = 0$, $\gamma = 0.006$.

of the vorticity obtained from the single passively flapping flag is displayed in figure 8(*b*), which assumed the 2P mode. For $f_{2h}/f_0 = 1.0$ and $G_x = 0.9$, i.e. the low-drag case in figure 7(*c*), figure 8(*c*) showed that the head of the downstream flag moved in between the pairs of vortices, i.e. the slalom mode. On the other hand, for $f_{2h}/f_0 = 1.0$ and $G_x = 1.4$ (figure 8*d*), i.e. the high-drag case in figure 7(*d*), the head of the downstream flag always passed across one of each pair of vortices, i.e. the interception mode. Similarly, time evolution of the vorticity at the middle position of the downstream flag is shown in figure 9. We can find the slalom mode (figure 9*c*) and the interception mode (figure 9*d*), corresponding to the reduced and enhanced flapping amplitudes, respectively. The difference between the two vortex–flag interaction modes is also displayed by the movies in the supplementary data available online at http://dx.doi.org/10.1017/jfm.2015.460.

The reason for inducing the low/high-drag force in the slalom/interception mode can be explained by the schematics in figure 10. For the slalom mode (figure 10*a*), the

https://doi.org/10.1017/jfm.2015.460 Published online by Cambridge University Press

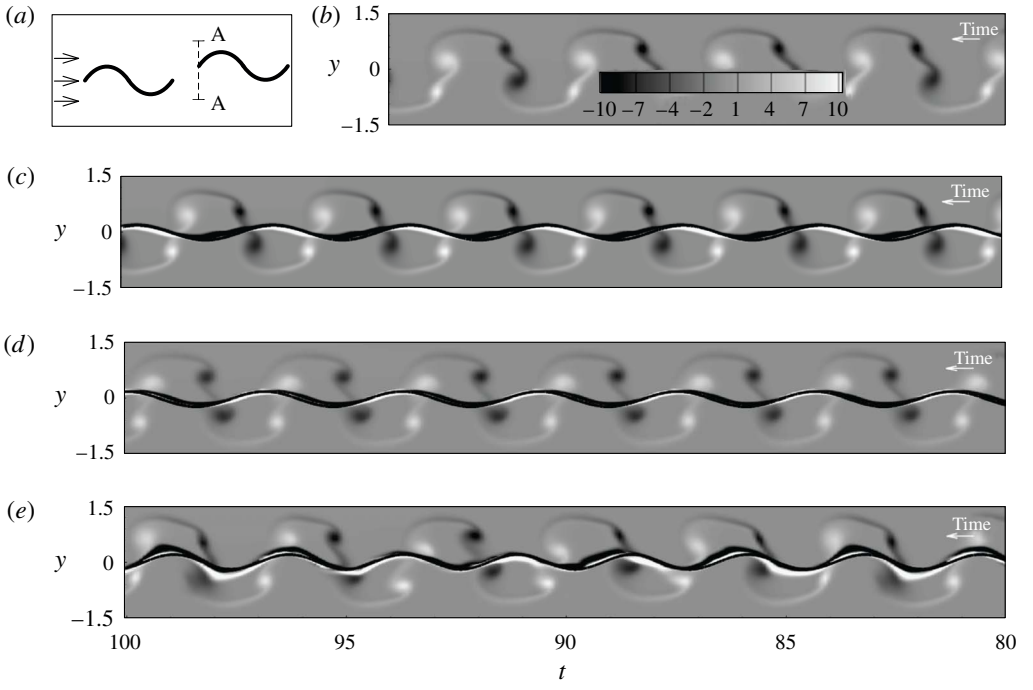


FIGURE 8. Time evolution of the vorticity along the vertical line at the head of the downstream flag, together with the trajectory of the head motion: (*a*) schematic diagram; (*b*) $f_{2h}/f_0 = 1.0$ for the single flag; (*c*) $f_{2h}/f_0 = 1.0$, $G_x = 0.9$; (*d*) $f_{2h}/f_0 = 1.0$, $G_x = 1.4$; (*e*) $f_{2h}/f_0 = 1.2$, $G_x = 1.0$.

head motion of the downstream flag (v_F) coincided with the vortex-induced velocity (v_Γ), while for the vortex interception mode (figure 10*b*), v_F was opposite to v_Γ in the y-direction. Note that the current mechanism discussed above was consistent with the findings of Liao *et al.* (2003) and Jia & Yin (2008), but was opposite to that of Zhu *et al.* (2014*c*). In Zhu *et al.* (2014*c*), the actively flapping flag with self-propulsion was prone to pass through the upstream vortices to save energy. It should be pointed out that such a difference was caused by the set-up of the problem. In the self-propulsion case, the reversed Karman vortex street was formed behind the upstream swimming body to generate the thrust, while the traditional Karman vortex street was attained in the drag wake of the passively flapping flag, pinned in the incoming flow. The above comparison showed the different natures of vortex–body interactions for fish swimming in different vortical environments.

For $f_{2h}/f_0 > 1.0$, the head of the downstream flag moved faster than the oncoming vortices. The interception of vortices by the downstream flag was always present, as seen in figure 11 for $f_{2h}/f_0 = 1.2$, and figures 8(*e*) and 9(*e*) as well. By further increasing the pitching and heaving frequency, more complicated vortex–body interactions were induced, and variation of the drag of the downstream flag with the gap distance became more irregular, as seen in figure 4(*d–f*). However, the increase in drag was mainly attributed to the pitching and heaving motions rather than the influence of the upstream shedding vortices. The reason can be seen by comparing the single and tandem cases in figure 2, and from the fact that the dominant frequency was the pitching and heaving frequency as $f_{2h}/f_0 > 1$ (see figure 3(*d–f*)). From the

https://doi.org/10.1017/jfm.2015.460 Published online by Cambridge University Press

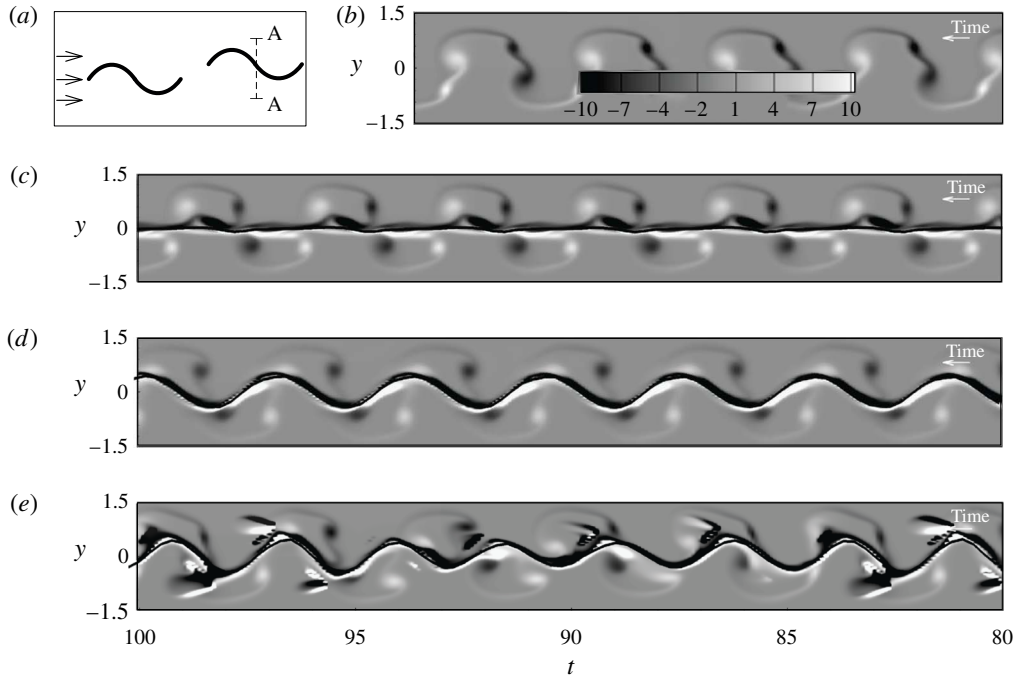


FIGURE 9. Time evolution of the vorticity along the vertical line through the middle point of the downstream flag, together with the trajectory of the middle point of the downstream flag: (*a*) schematic diagram; (*b*) $f_{2h}/f_0 = 1.0$ for the single flag; (*c*) $f_{2h}/f_0 = 1.0$, $G_x = 0.9$; (*d*) $f_{2h}/f_0 = 1.0$, $G_x = 1.4$; (*e*) $f_{2h}/f_0 = 1.2$, $G_x = 1.0$.

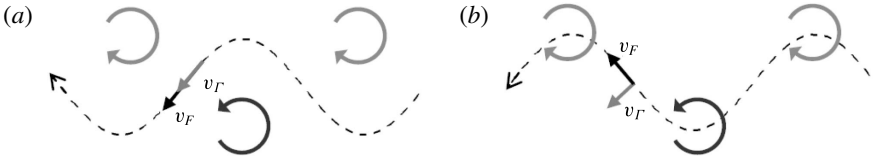


FIGURE 10. Schematics of (*a*) the slalom mode and (*b*) the interception mode. The central dashed line denotes the trajectory of the head motion. The circles with arrows denote the vortices. v_F denotes the velocity of the head motion and v_Γ denotes the vortex-induced velocity.

energetic point of view, the head motion of the downstream flag with a frequency higher than the upstream shedding vortices was not found for a stably swimming fish under the influence of the vortical wake.

In the following, the effects of the phase angles $\Phi_{pitching}$ and $\Phi_{heaving}$, and the pitching and heaving amplitudes Θ and Y, were examined. Figure 12 shows the contours of the drag coefficient of the downstream flag, C_{d2}, as a function of $\Phi_{pitching}$ and $\Phi_{heaving}$ for $G_x = \infty$ and $G_x = 1.0$ at $f_{2h}/f_0 = 1.0$, respectively, and those of Θ and Y are plotted in figure 13. More than 400 points were included in each map. It is interesting to see in figure 12(*a*) that for the single pitching and heaving flag, the contours of C_d displayed a regular pattern and reached a minimum for $\Phi_{pitching} - \Phi_{heaving} = 0.75\pi$ and a maximum for $\Phi_{pitching} - \Phi_{heaving} = -0.25\pi$. Thus, C_d of the single pitching and heaving flag depended only on the phase difference

https://doi.org/10.1017/jfm.2015.460 Published online by Cambridge University Press

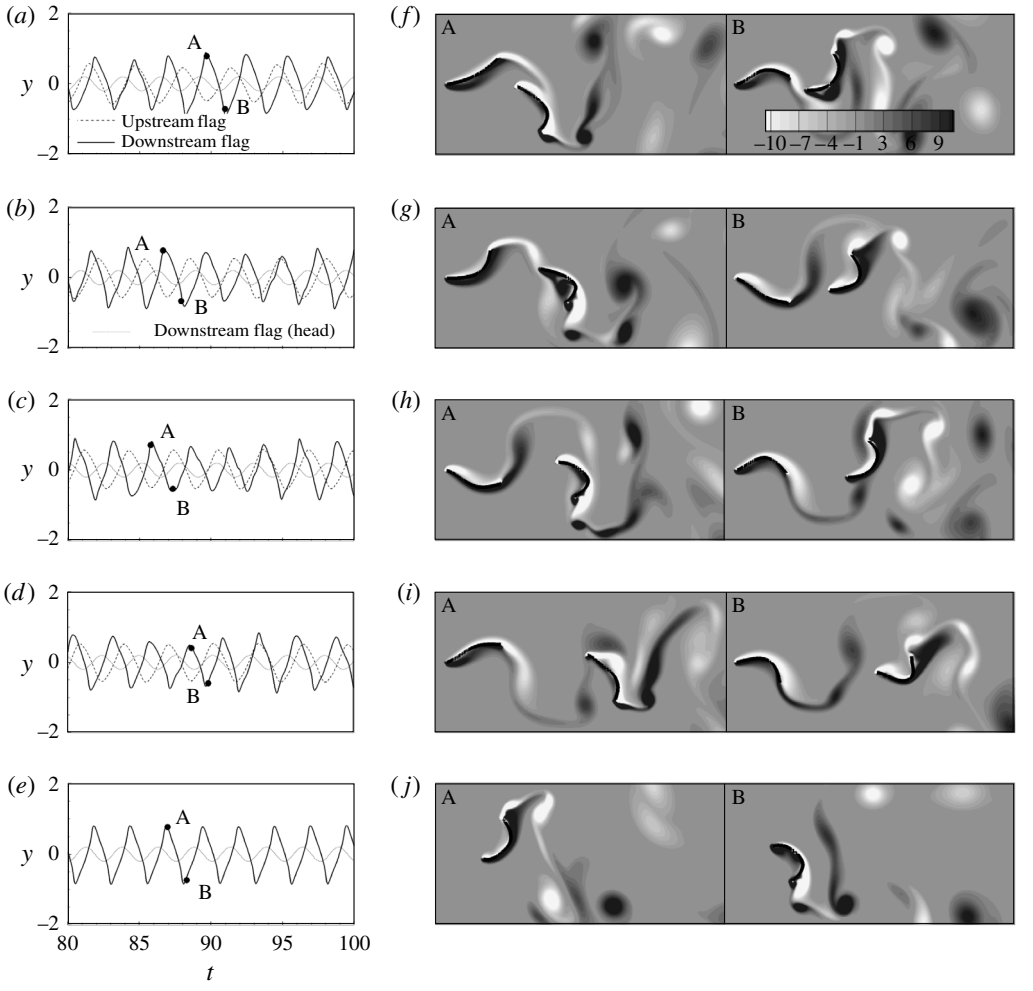


FIGURE 11. For comparison to the plots shown in figures 5 and 7. Time histories of the head and tail positions (*a–e*) and vorticity contours, together with the body shape (*f–j*) at $f_{2h}/f_0 = 1.2$ (rather than for $f_{2h}/f_0 = 0.3$, in figure 5): (*a*) $G_x = 0.2$; (*b*) $G_x = 0.6$; (*c*) $G_x = 1.0$; (*d*) $G_x = 1.4$; (*e*) $G_x = \infty$.

between the pitching and heaving motions. However, the difference in C_d was small as shown in figure 12(*a*). The superimposition of the body shapes in figure 14 displayed a similar pattern for both the low- and high-drag cases as labelled by the points 'a' and 'b' in figure 12(*a*), respectively. The vortex pattern from the trailing edge of the single flapping flag was similar, although the body kinematics differed. For the tandem flag system (figure 12*b*), the significant difference in C_{d2} resulted from the difference in the phase angle. Although an inclined striped pattern was roughly seen, C_{d2} was affected by $\Phi_{heaving}$ rather than $\Phi_{pitching}$. The body shapes for the low- and high-drag cases are labelled by points 'c' and 'd' in figure 12(*b*) respectively. Different envelopes are displayed in figure 14 despite the same heaving amplitude. The vortex–flag interactions shown in figure 15(*a*) and (*b*) represent the slalom mode and the interception mode, respectively.

https://doi.org/10.1017/jfm.2015.460 Published online by Cambridge University Press

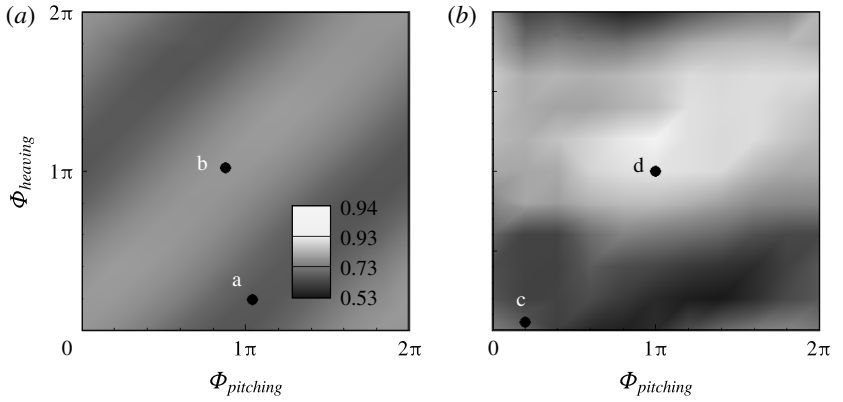


FIGURE 12. Contours of the drag coefficients of the downstream flag as a function of the phase angles of the pitching and heaving motion at $f_{2h}/f_0 = 1.0$: (*a*) $G_x = \infty$ for the single flag; (*b*) $G_x = 1.0$. Other parameters were $Re = 300$, $Y = 0.2$, $\Theta = 0.1\pi$, $\gamma = 0.006$.

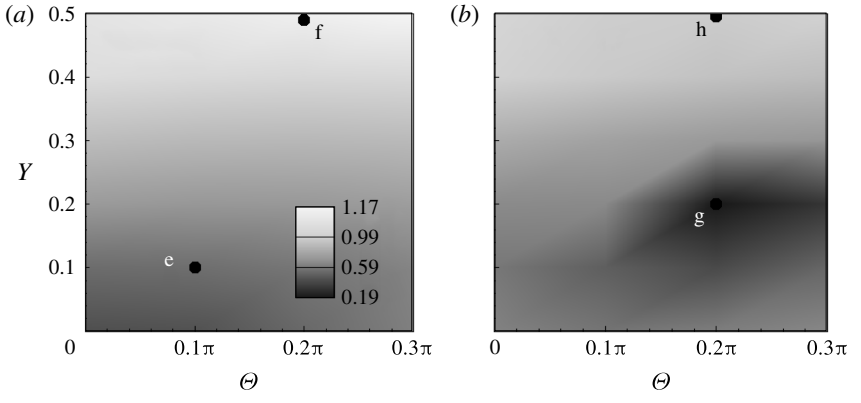


FIGURE 13. Contours of the drag coefficient of the downstream flag as a function of the amplitude of the pitching and heaving motion at $f_{2h}/f_0 = 1.0$: (*a*) $G_x = \infty$ for the single flag; (*b*) $G_x = 1.0$.

The influence of the pitching and heaving amplitudes Θ and Y on C_d is plotted in figure 13 for both the single ($G_x = \infty$) and tandem ($G_x = 1.0$) cases at $f_{2h}/f_0 = 1.0$. In general, the drag coefficient was more affected by the heaving amplitude. Due to the fast motion of the head of the downstream flag, the lateral displacement significantly affected the body shape and the leading edge vortices. For the single-flag system, C_d increased monotonically with the heaving amplitude (figure 13*a*), and the body shape was significantly affected by the heaving amplitude (see the points 'e' and 'f' in figure 14). On the other hand, for the tandem case, C_{d2} decreased significantly within a certain region of Y and Θ (figure 13*b*), as did the flapping amplitude for the body shapes, i.e. the points 'g' and 'h' in figure 14. An appropriate pitching and heaving amplitude was in favour of the vortex–flag interactions for drag reduction. The body shape of point 'g' showed an asymmetric pattern, which can also be seen in the time history of the downstream tail motion in figure 7(*c*). Such an asymmetric pattern was displayed only in specific cases of phase difference and flapping amplitude. This may be induced by the vortex locking behaviour due to the same flapping frequency as the

https://doi.org/10.1017/jfm.2015.460 Published online by Cambridge University Press

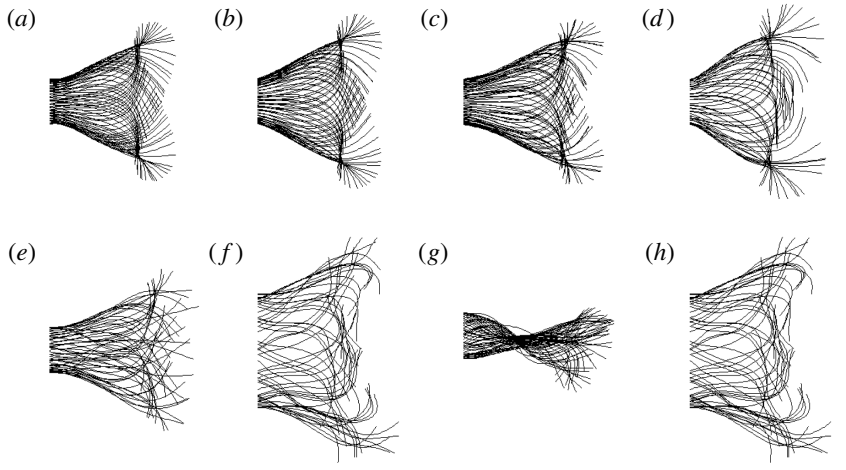


FIGURE 14. Superimposition of the body shapes of the downstream flag. The numbering is sequentially labelled in figures 12 and 13.

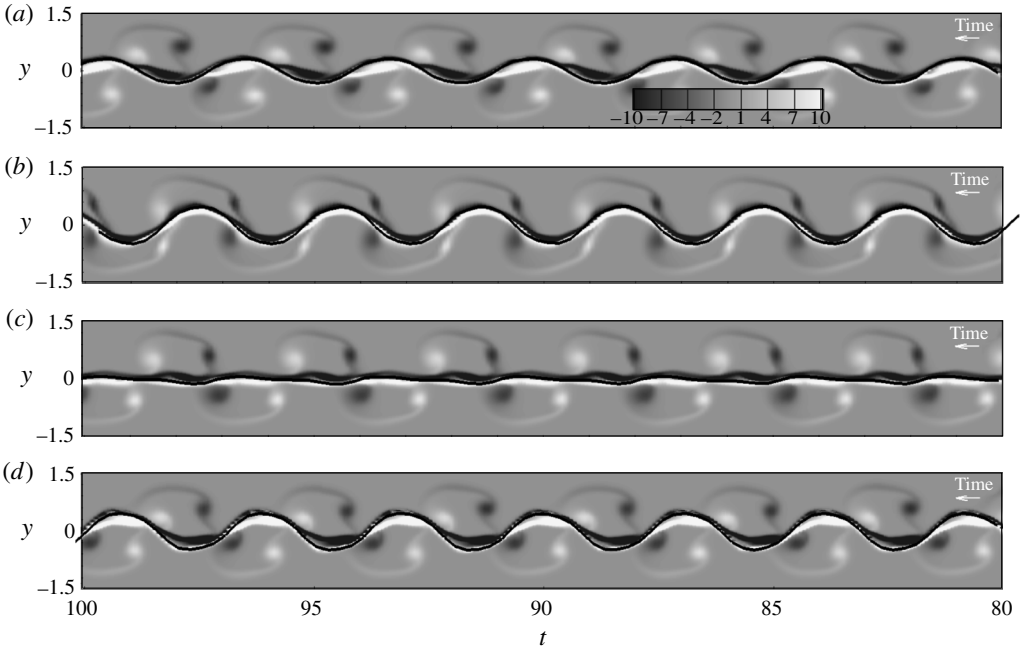


FIGURE 15. Time evolution of the vorticity along the vertical line in the middle point of the downstream flag, together with the trajectory of the middle point of the downstream flag. (*a*) Point 'c'; (*b*) point 'd'; (*c*) point 'g'; (*d*) point 'h'. Points 'c' and 'd' are labelled in figure 12 and points 'g' and 'h' in figure 13.

upstream vortex shedding frequency. Evolution of the vorticity in the middle of the downstream flag in figure 15(*c*) and (*d*) demonstrated that the slalom and interception modes corresponded to the low- and high-drag forces, respectively. At this frequency ratio, a single fish was expected to suppress the heaving amplitude to reduce drag,

https://doi.org/10.1017/jfm.2015.460 Published online by Cambridge University Press

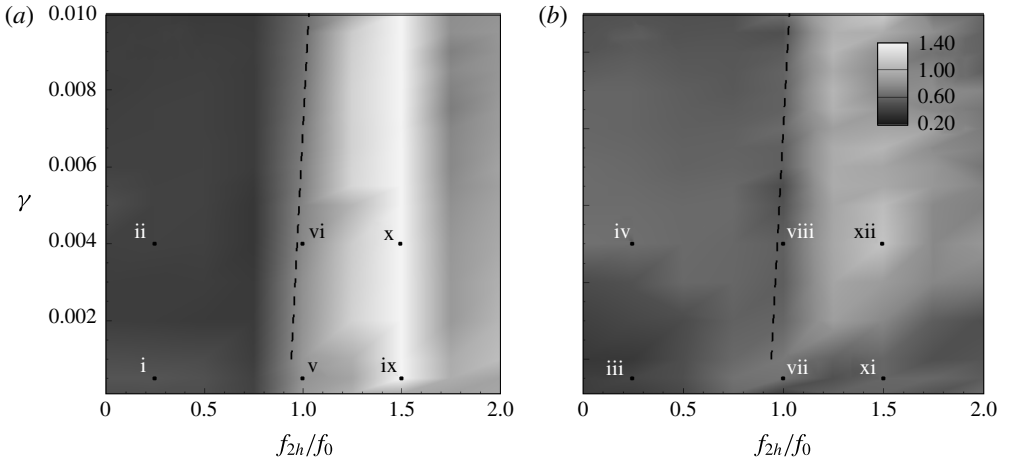


FIGURE 16. Contours of C_d of the downstream flag as a function of the bending coefficient and the flapping frequency: (*a*) $G_x = \infty$ for the single flag; (*b*) $G_x = 1.0$. The dashed line denotes the location of the natural flapping frequency for $Re = 300$, $Y = 0.2$, $\Theta = 0.1\pi$, $\Phi_{pitching} = 0.5\pi$ and $\Phi_{heaving} = 0$.

but fish swimming in the environment formed by the vortices shed from the upstream body tended to optimize its pitching and heaving amplitudes.

Finally, the influence of the bending coefficient on the system dynamics was explored. Figure 16 shows the contours of C_d of the downstream flag and the single flapping flag as a function of the bending coefficient γ and the flapping frequency f_{2h} within the ranges $10^{-4} \leqslant \gamma \leqslant 10^{-2}$ and $0 \leqslant f_{2h}/f_0 \leqslant 2$. Note that the natural flapping frequency f_0 is weakly dependent on the bending coefficient. For consistency, here we still use f_0 at $\gamma = 0.006$ for the normalization of f_{2h}. In figure 16, the inclined dashed line across $f_{2h}/f_0 = 1$ indicates that f_0 increased slightly with γ. For the single pitching and heaving flag in figure 16(*a*), C_d changed little by varying γ, but it changed significantly by varying the flapping frequency, as shown in figure 2. To see this more clearly, the curves of C_d as a function of γ for different f_{2h}/f_0 are plotted in figure 17. Within the range of γ considered in the present study, variations of C_d of the single flag were small for each flapping frequency. Figure 18 presents the superimposition of the body shape of the flag within a flapping period for the points labelled in figure 16. Similar patterns of the body shapes, as well as the flapping amplitudes of the tail, were observed by comparing the single-flag cases with different γ, i.e. point 'i' versus 'ii', 'v' versus 'vi', and 'ix' versus 'x'.

For the tandem case, the flapping motion of the downstream flag became more complicated due to the influence of the upstream shedding vortices. As seen in figure 16(*b*), C_{d2} remained almost unchanged with γ in a wide range, i.e. $2 \times 10^{-3} \leqslant \gamma \leqslant 10^{-2}$. The variation of C_{d2} with the frequency ratio within this range was examined in detail. However, different behaviours were observed for the downstream flag with a small bending coefficient. We can see that C_{d2} changed little for $\gamma \leqslant 2 \times 10^{-3}$ and all frequency ratios except near $f_{2h}/f_0 = 1$. For $f_{2h}/f_0 < 1$, C_{d2} was comparable to C_{d1} for $\gamma \leqslant 2 \times 10^{-3}$ and was slightly increased for $2 \times 10^{-3} \leqslant \gamma \leqslant 10^{-2}$ according to figures 17(*a*) and (*b*). The body shape of point 'iv' labelled in figure 16(*b*) displayed a slightly more expanded envelope than that of point 'iii', as seen in figure 18. Figure 19 shows the power spectra of the tail position of

https://doi.org/10.1017/jfm.2015.460 Published online by Cambridge University Press

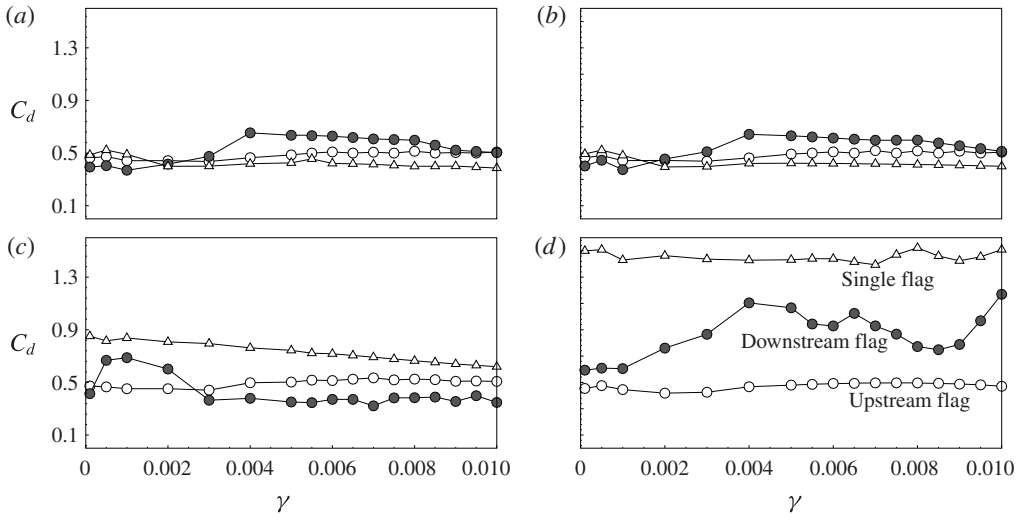


FIGURE 17. The drag coefficient as a function of the bending coefficient at different flapping frequencies: (*a*) $f_{2h}/f_0 = 0$; (*b*) $f_{2h}/f_0 = 0.25$; (*c*) $f_{2h}/f_0 = 1.0$; (*d*) $f_{2h}/f_0 = 1.5$. Also, (*a*) $\Phi = 0.1\pi$, $Y = 0.2$; (*b*) $Re = 300$, $G_x = 1.0$; (*c*) $\Phi_{pitching} = 0.5\pi$, $\Phi_{heaving} = 0.0$.

the downstream flag for the points labelled in figure 16. For point 'iii', the spectrum peak at the natural flapping frequency was comparable to that at the pitching and heaving frequency. However, the peak at the natural flapping frequency was dominant for point 'iv'. As discussed above, the modulation of the upstream shedding vortices was obvious when $f_{2h}/f_0 < 1$. The difference in the spectra between points 'iii' and 'iv' indicates that the modulation effect was suppressed by the body deformation with a very low bending rigidity flapping at a low frequency. On the other hand, for $f_{2h}/f_0 > 1$, C_{d2} was also comparable to C_{d1} for $\gamma \leqslant 2 \times 10^{-3}$. However, a significant increase in C_{d2} was observed for larger γ in figure 17(*d*). As mentioned earlier, a high flapping frequency usually resulted in the interception mode. Exceptions were observed for $\gamma \leqslant 2 \times 10^{-3}$, where C_{d2} remained low even for $f_{2h}/f_0 > 1$. In figure 18, the body shape of point 'xi' labelled in figure 16(*b*) showed significant difference from that of point 'xii', implying the influence of the upstream shedding vortices. As seen in figure 19(*c*), the spectrum of point 'xi' showed that the spectrum peak at the natural frequency was comparable to that at the flapping frequency. Unlike the spectrum of point 'xii', where the peak at the flapping frequency was dominant, we found a clear feature of the interception mode. For $f_{2h}/f_0 = 1$, an increase in C_{d2} was observed for $\gamma \leqslant 2 \times 10^{-3}$, and a decrease elsewhere (figure 17*c*). The decrease in C_{d2} was caused by the slalom mode due to the interaction with upcoming vortices. For very flexible flags at $f_{2h}/f_0 = 1$, although the superimpositions of the body shapes and the power spectrum were found to be similar to those of more rigid flags by comparing points 'vii' and 'viii' in figures 18 and 19(*c*), the plots of vorticity evolution show that the interception mode was formed for the low bending case and the slalom mode for the more rigid flag, as seen in figure 20.

4. Conclusions

The present study examined the dynamics of tandem flexible flags in a viscous flow under prescribed active pitching and heaving motions applied to the head of the

https://doi.org/10.1017/jfm.2015.460 Published online by Cambridge University Press

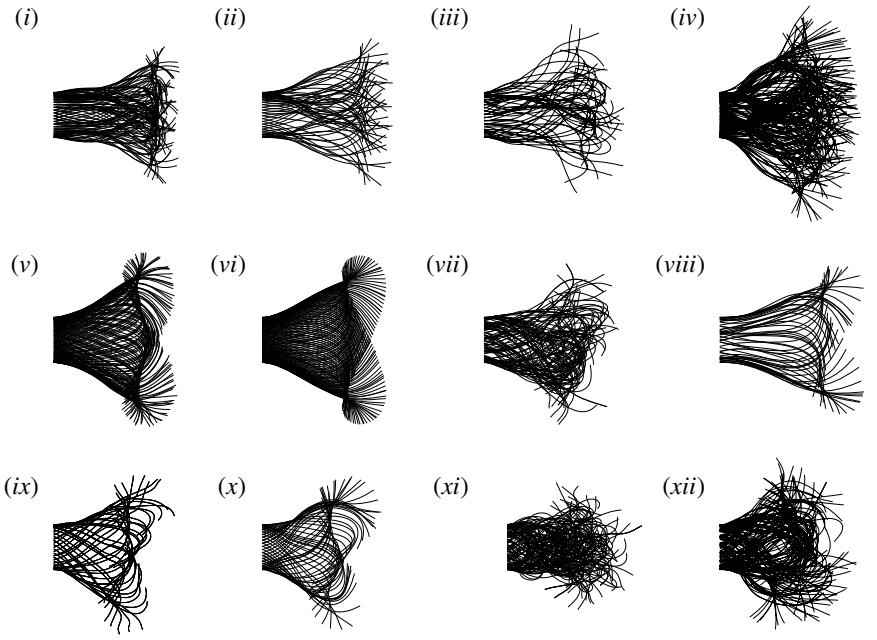


FIGURE 18. Superimposition of the body shapes of the downstream flag. The numbering is sequentially labelled in figure 16.

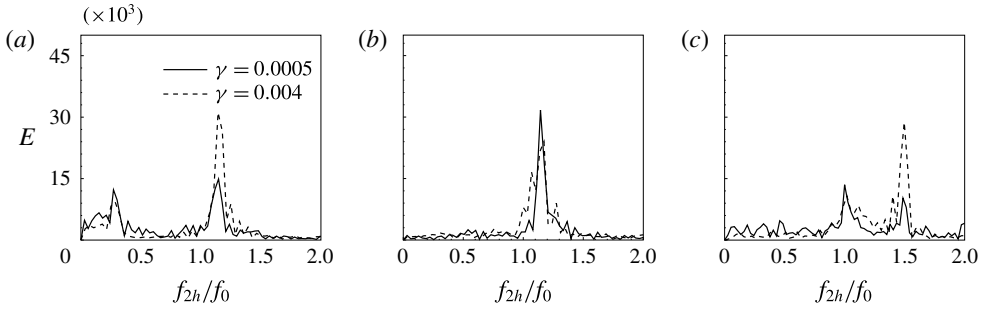


FIGURE 19. Power spectra of the tail positions for different points labelled in figure 16: (*a*) iii and iv; (*b*) vii and viii; (*c*) xi and xii. Also, (*a*) $f_{2h}/f_0 = 0.25$; (*b*) $f_{2h}/f_0 = 1.0$, $\Phi_{pitching} = 0.5\pi$, $\Phi_{heaving} = 0$; (*c*) $f_{2h}/f_0 = 1.5$, $Re = 300$, $\Phi = 0.1\pi$, $G_x = 1.0$, $Y = 0.2$.

downstream flag. The effects of various parameters on the dynamics were explored, including the flapping frequency, the gap distance, the pitching and heaving phase angles and amplitudes, and the bending coefficient. Special attention has been paid to the underlying mechanism related to the status of the downstream flag motion, and some interesting features of the dynamic system were explored:

(1) When the enforced flapping frequency was less than the natural flapping frequency, the modulation of the upstream shedding vortices with the downstream flag motion was observed, and the drag of the downstream flag was only slightly dependent on the gap distance between the two flags. The phase difference between the tail motions of the upstream and downstream flags increased linearly

https://doi.org/10.1017/jfm.2015.460 Published online by Cambridge University Press

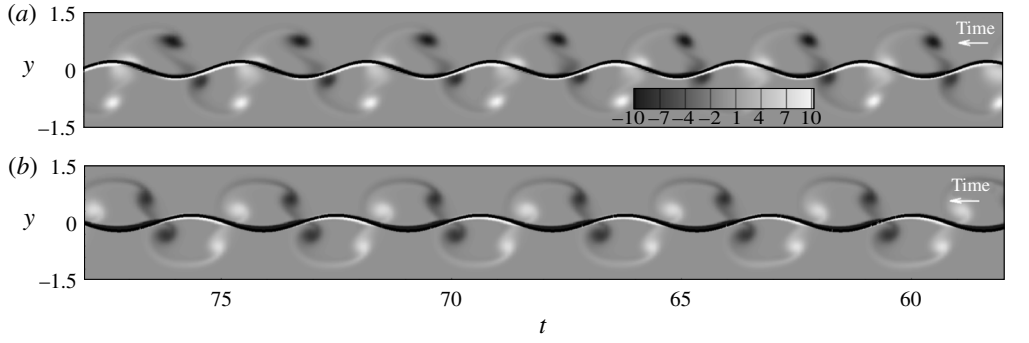


FIGURE 20. Time evolution of the vorticity along the vertical line at the head of the downstream flag, together with the trajectory of the middle point of the downstream flag. (*a*) Point 'vii'; (*b*) point 'viii'. Points 'vii' and 'viii' are labelled in figure 16.

with the gap distance, since the propagation time for the vortices arriving at the downstream flag was proportional to the gap distance. The power spectrum of the tail position of the downstream flag indicated that the natural frequency was dominant due to the modulation effect.

(2) When the enforced flapping frequency was equal to the natural flapping frequency, besides the constructive mode of the passive flapping case, different modes, i.e. the slalom mode and the interception mode, were identified by varying the gap distance. The drag was reduced for the slalom mode but was increased for the interception mode. A simplified physical model was provided to explain the intrinsic mechanism, and comparison with previous studies was discussed.

(3) When the enforced flapping frequency was larger than the natural flapping frequency the interception mode was generally observed. The drag of the downstream flag was significantly increased as compared with the upstream one. The power spectra of the tail position of the downstream flag showed that the enforced frequency was dominant over the natural flapping frequency. From the energetic point of view, the head motion of the downstream flag with a frequency higher than the upstream shedding vortices was not usually observed for a stably swimming fish under the influence of the vortical wake.

(4) At specific flapping frequencies and gap distances, the pitching and heaving phase angles and amplitudes were examined systematically. For the single pitching and heaving flag, the drag showed a regular pattern with the pitching and heaving phase angles, depending only upon the phase difference. The drag was increased with the heaving amplitude but insensitive to the pitching amplitude. For the tandem flag system, the heaving phase had a more significant influence on the drag of the downstream flag than the pitching phase, by adjusting the relative position of the head and the oncoming vortices. The drag was minimized over a certain range of the pitching and heaving amplitudes, suggesting that the fish might adjust its head motion to adapt to the oncoming vortical wake so as to minimize its drag.

(5) Within a certain range of the bending coefficient considered in the present study, the drag of the downstream flag was found to be almost independent of the bending coefficient, but to vary significantly with the flapping frequency.

https://doi.org/10.1017/jfm.2015.460 Published online by Cambridge University Press

However, for very low bending rigidities, different behaviours were found for the downstream flag. The power spectra of the tail positions showed that the peak at the natural frequency was comparable with that at the enforced flapping frequency. The modulation effect was diminished due to the too flexible body at low flapping frequencies, while the flapping elastic energy was small at high flapping frequencies, as compared with the more rigid cases. As a result, by bearing a small bending rigidity, the drag of the downstream flag always remained low and comparable with the upstream one. An exception was observed near the frequency ratio equal to one, where the interception mode was formed and the drag was increased for low bending rigidities, which is opposite to the slalom mode for the more rigid cases.

Acknowledgements

This work was supported by the Creative Research Initiatives (no. 2015-01828) programme of the National Research Foundation of Korea (MSIP). W.-X.H. acknowledges the support from the NSFC (no. 11322221).

Supplementary movies

Supplementary movies are available at http://dx.doi.org/10.1017/jfm.2015.460.

REFERENCES

ALBEN, S. 2009 Wake-mediated synchronization and drafting in coupled flags. *J. Fluid Mech.* **641**, 489–496.

ALBEN, S. 2011 Flapping propulsion using a fin ray. *J. Fluid Mech.* **705**, 149–164.

ALBEN, S., MADDEN, P. G. & LAUDER, G. V. 2007 The mechanics of active fin-shape control in ray-finned fishes. *J. R. Soc. Interface* **4** (12), 243–256.

ALBEN, S., WITT, C., BAKER, T. V., ANDERSON, E. & LAUDER, G. V. 2012 Dynamics of freely swimming flexible foils. *Phys. Fluids* **24**, 051901.

AKHTAR, I., MITTAL, R., LAUDER, G. V. & DRUCKER, E. 2007 Hydrodynamics of a biologically inspired tandem flapping foil configuration. *Theor. Comput. Fluid Dyn.* **21**, 155–170.

ANDERSON, J. M., STREITLIEN, K., BARRETT, D. S. & TRIANTAFYLLOU, M. S. 1998 Oscillating foils of high propulsive efficiency. *J. Fluid Mech.* **360**, 41–72.

BEAL, D. N., HOVER, F. S., TRIANTAFYLLOU, M. S., LIAO, J. C. & LAUDER, G. V. 2006 Passive propulsion in vortex wakes. *J. Fluid Mech.* **549**, 385–402.

DENG, H.-B., XU, Y.-Q., CHEN, D.-D., DAI, H., WU, J. & TIAN, F.-B. 2013 On numerical modeling of animal swimming and flight. *Comput. Mech.* **52**, 1221–1242.

ELOY, C. & LAUGA, E. 2012 Kinematics of the most efficient cilium. *Phys. Rev. Lett.* **109**, 038101.

FISH, F. E. & LAUDER, G. V. 2006 Passive and active flow control by swimming fishes and mammals. *Annu. Rev. Fluid Mech.* **38**, 193–224.

GOPALKRISHNAN, R., TRIANTAFYLLOU, M. S., TRIANTAFYLLOU, G. S. & BARRETT, D. 1994 Active vorticity control in a shear flow using a flapping foil. *J. Fluid Mech.* **274**, 1–21.

GUGLIELMINI, L. & BLONDEAUX, P. 2004 Propulsive efficiency of oscillating foils. *Eur. J. Mech. (B/Fluids)* **23**, 255–278.

HUANG, W.-X., SHIN, S. J. & SUNG, H. J. 2007 Simulation of flexible filaments in a uniform flow by the immersed boundary method. *J. Comput. Phys.* **226**, 2206–2228.

HUANG, W.-X. & SUNG, H. J. 2009 An immersed boundary method for fluid-flexible structure interaction. *Comput. Meth. Appl. Mech. Engng* **198**, 2650–2661.

JIA, L. B. & YIN, X. Y. 2008 Passive oscillations of two tandem flexible filaments in a flowing soap film. *Phys. Rev. Lett.* **100**, 228104.

https://doi.org/10.1017/jfm.2015.460 Published online by Cambridge University Press

KANG, C. K., AONO, H., CESNIK, C. E. S. & SHYLY, W. 2011 Effects of flexibility on the aerodynamic performance of flapping wings. *J. Fluid Mech.* **689**, 32–74.

KIM, K., BAEK, S.-J. & SUNG, H. J. 2002 An implicit velocity decoupling procedure for the incompressible Navier–Stokes equations. *Intl J. Numer. Meth. Fluids* **38**, 125–138.

KIM, S., HUANG, W.-X. & SUNG, H. J. 2010 Constructive and destructive interaction modes between two tandem flexible flags in viscous flow. *J. Fluid Mech.* **661**, 511–521.

LAUDER, G. V., ANDERSON, E. J., TANGORRA, J. & MADDEN, P. G. 2007 Fish biorobotics: kinematics and hydrodynamics of self-propulsion. *J. Expl Biol.* **210**, 2767–2780.

LIAO, J. C., BEAL, D. N., LAUDER, G. V. & TRIANTAFYLLOU, M. S. 2003 Fish exploiting vortices decrease muscle activity. *Science* **302**, 1566–1569.

LIGHTHILL, M. J. 1970 Aquatic animal propulsion of high hydromechanical efficiency. *J. Fluid Mech.* **44**, 265–301.

MARAIS, C., THIRIA, B., WESFREID, J. E. & GODOY-DIANA, R. 2012 Stabilizing effect of flexibility in the wake of a flapping foil. *J. Fluid Mech.* **710**, 659–669.

MASOUD, H. & ALEXEEV, A. 2010 Resonance of flexible flapping wings at low Reynolds number. *Phys. Rev.* E **81**, 056304.

MICHELIN, S. & SMITH, S. G. L. 2009 Resonance and propulsion performance of a heaving flexible wing. *Phys. Fluids* **21**, 071902.

RAMANANARIVO, S., GODOY-DIANA, R. & THIRIA, B. 2011 Rather than resonance, flapping wing flyers may play on aerodynamics to improve performance. *Proc. Natl Acad. Sci. USA* **108**, 5964–5969.

RISTROPH, L. & ZHANG, J. 2008 Anomalous hydrodynamic drafting of interacting flapping flags. *Phys. Rev. Lett.* **101**, 194502.

SHELLEY, M. J. & ZHANG, J. 2011 Flapping and bending bodies interacting with fluid flows. *Annu. Rev. Fluid Mech.* **43**, 449–465.

SHIN, S. J., HUANG, W.-X. & SUNG, H. J. 2008 Assessment of regularized delta functions and feedback forcing schemes for an immersed boundary method. *Intl J. Numer. Meth. Fluids* **58**, 263–286.

SHOELE, K. & ZHU, Q. 2012 Leading edge strengthening and the propulsion performance of flexible ray fins. *J. Fluid Mech.* **693**, 402–432.

SHYY, W., AONO, H., CHIMAKURTHI, S. K., TRIZILA, P., KANG, C.-K., CESNIK, C. E. S. & LIU, H. 2010 Recent progress in flapping wing aerodynamics and aeroelasticity. *Prog. Aerosp. Sci.* **46**, 284–327.

SPAGNOLIE, S. E., MORET, L., SHELLEY, M. J. & ZHANG, J. 2010 Surprising behaviors in flapping locomotion with passive pitching. *Phys. Fluids* **22**, 041903.

THIRIA, B. & GODOY-DIANA, R. 2010 How wing compliance drives the efficiency of self-propelled flapping flyers. *Phys. Rev.* E **82**, 015303(R).

TUNCER, I. H. & KAYA, M. 2005 Optimization of flapping airfoils for maximum thrust and propulsive efficiency. *AIAA J.* **43** (11), 2329–2336.

UDDIN, E., HUANG, W.-X. & SUNG, H. J. 2013 Interaction modes of multiple flexible flags in a uniform flow. *J. Fluid Mech.* **729**, 563–583.

WANG, Z. J. 2005 Dissecting insect flight. *Annu. Rev. Fluid Mech.* **37**, 183–210.

WILLIAMSON, C. H. K. & GOVARDHAN, R. 2004 Vortex-induced vibrations. *Annu. Rev. Fluid Mech.* **36**, 413–455.

WU, T. Y. 2011 Fish swimming and bird/insect flight. *Annu. Rev. Fluid Mech.* **43**, 25–58.

ZHANG, J., CHILDRESS, S., LIBCHABER, A. & SHELLEY, M. 2000 Flexible filaments in a flowing soap film as a model for one-dimensional flags in a two-dimensional wind. *Nature* **408**, 835–839.

ZHU, L. 2009 Interaction of two tandem deformable bodies in a viscous incompressible flow. *J. Fluid Mech.* **635**, 455–475.

ZHU, X., HE, G. & ZHANG, X. 2014*a* Numerical study on hydrodynamic effect of flexibility in a self-propelled plunging foil. *Comput. Fluids* **97**, 1–20.

https://doi.org/10.1017/jfm.2015.460 Published online by Cambridge University Press

ZHU, X., HE, G. & ZHANG, X. 2014*b* How flexibility affects the wake symmetry properties of a self-propelled plunging foil. *J. Fluid Mech.* **751**, 164–183.

ZHU, X., HE, G. & ZHANG, X. 2014*c* Flow-mediated interactions between two self-propelled flapping filaments in tandem configuration. *Phys. Rev. Lett.* **113**, 238105.

https://doi.org/10.1017/jfm.2015.460 Published online by Cambridge University Press